$CH_3^\bullet$ Is Planar Due to H−H Steric Repulsion. Theoretical Study of $MH_3^\bullet$ and MH_3Cl (M = C, Si, Ge, Sn)

F. Matthias Bickelhaupt,*,† Tom Ziegler,* and Paul von Ragué Schleyer‡

Department of Chemistry, University of Calgary, Calgary, Alberta, Canada T2N 1N4

Received July 21, 1995⊗

The molecular structure and bonding mechanisms of $MH_3^\bullet$ radicals and MH_3Cl (M = C, Si, Ge, Sn) have been studied with the use of local (LDA) as well as nonlocal (NL-SCF) density-functional theory (DFT) and a large, doubly polarized triple-ζ STO basis (TZ2P). The $CH_3^\bullet$ radical is planar (D_{3h}) whereas the heavier central atom analogs are pyramidal: the H−M−H bond angle β (=120.00, 112.66, 112.44, 110.56°) decreases, and the inversion barrier ΔE_{inv} + ΔZPE (=0.0, 3.7, 3.8, 7.0 kcal/mol) increases along the series $CH_3^\bullet$, $SiH_3^\bullet$, $GeH_3^\bullet$, and $SnH_3^\bullet$ (NL-SCF/TZ2P). The homolytic M−Cl bond dissociation energy D_{homo} + ΔZPE is 81.7, 105.6, 96.2, and 93.6 kcal/mol for CH_3−Cl, SiH_3−Cl, GeH_3−Cl, and SnH_3−Cl, respectively (NL-SCF/TZ2P). A detailed analysis of the bonding mechanisms shows that the $CH_3^\bullet$ radical is planar because of the steric repulsion between the hydrogen ligands. This steric H−H repulsion is much weaker for $SiH_3^\bullet$, $GeH_3^\bullet$, and $SnH_3^\bullet$ in which the ligands are farther removed from each other. Electronic effects (i.e. electron pair bonding between the central atom and hydrogen ligands) always favor a pyramidal structure, although only slightly so for the methyl radical. The analysis of the MH_3−Cl bond reveals that initially the bond strength increases with the increasing M−Cl electronegativity difference (from M = C to Si) and then decreases together with the bond overlap between the $MH_3^\bullet$ and $Cl^\bullet$ SOMOs (from Si to Sn). The results are discussed in the context of those previously obtained for the complementary series of the CH_3−X bond (X = F, Cl, Br, I) to provide a more complete insight into the electronic structure and bonding of the archetype MH_3X molecule.

1. Introduction

Halomethanes and their heavier central atom homologs (MH_3X, Chart 1) are archetypes of substituted (in)organic molecules.[1] Compounds containing an M−X bond are furthermore involved in many organic and organometallic standard reactions.[1] Therefore, the experimental[2−4] and theoretical[5,6] investigation of MH_3X systems and the M−X bond has contributed much to the understanding and development of both structural and synthetic chemistry. The pronounced elongation of M−X and M−H bonds as well as the (slightly) increasing degree of pyramidalization of the MH_3 fragment when M varies from carbon to a heavier group 14 atom are general structural trends (*vide infra*). The decreasing CH_3−X bond strength along X = F, Cl, Br, and I was shown by Deng *et al.*[5] to be due to the decreasing difference in electronegativity between C and X and the associated decrease in charge transfer. The homolytic MH_3−Cl bond strength, on the other hand, increases

Chart 1

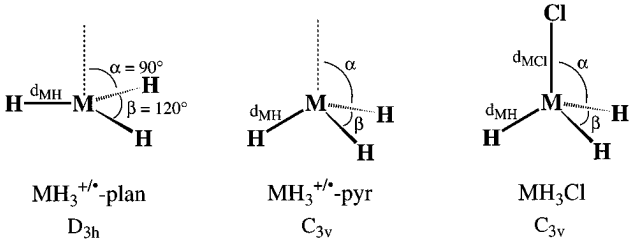

† Present address: Baker Laboratory, Department of Chemistry, Cornell University, Ithaca, NY 14853-1301.

‡ Computer-Chemie-Centrum, Universität Erlangen-Nürnberg, Nägelsbachstrasse 25, D-91052 Erlangen, Germany.

⊗ Abstract published in *Advance ACS Abstracts,* February 1, 1996.

(1) (a) March, J. *Advanced Organic Chemistry;* Wiley-Interscience: New York, 1992. (b) Carey, F. A.; Sundberg, R. J. *Advanced Organic Chemistry, Part A;* Plenum Press: New York, 1984. (c) Elschenbroich, Ch.; Salzer, A. *Organometallics. A Concise Introduction,* 2nd ed.; VCH: Weinheim, Germany, 1992. (d) Collman, J. P.; Hegedus, L. S.; Norton, J. R.; Finke, R. G. *Principles and Applications of Organotransition Metal Chemistry;* University Science Books: Mill Valley, CA, 1987.

(2) (a) Bürger, H.; Betzel, M.; Schultz, P. *J. Mol. Spetrosc.* **1987**, *121*, 218. (b) Cradock, S.; McKean, D. C.; MacKenzie, M. W. *J. Mol. Struct.* **1981**, *74*, 265. (c) Harmony, M. D.; Laurie, V. W.; Kuczkowski, R. L.; Schwendeman, R. H.; Ramsay, D. A.; Lovas, F. J.; Lafferty, W. J.; Maki, A. G. *J. Phys. Chem. Ref. Data* **1979**, *8*, 619. (d) Callomon, J. H.; Hirota, E.; Kuchitsu, K.; Lafferty, W. J.; Maki, A. G.; Pote, C. S. In *Strukturdaten freier mehratomiger Molekeln, Landolt-Börnstein, Neue Serie, Gruppe II: Atom- und Molekularphysik, Band 7;* Hellwege, K.-H.; Hellwege, A. M., Eds.; Springer-Verlag: Berlin, 1976.

(3) (a) Lias, S. G.; Bartmess, J. E.; Liebman, J. F.; Holmes, J. L.; Levin, R. D.; Mallard, W. G. *J. Phys. Chem. Ref. Data* **1988**, *17*, Suppl. No. 1. (b) *CRC Handbook of Chemistry and Physics*, 63rd ed.; Weast, R. C., Ed.; CRC Press: Boca Raton, FL, 1982; p D-195.

(4) (a) Sita, L. R. *Acc. Chem. Res.* **1994**, *27*, 191. (b) Walsh, R. *Acc. Chem. Res.* **1981**, *14*, 246.

(5) (a) Deng, L.; Branchadell, V.; Ziegler, T. *J. Am. Chem. Soc.* **1994**, *116*, 10645. (b) Fujimoto, H.; Satoh, S. *J. Phys. Chem.* **1994**, *98*, 1436. (c) Pearson, R. G. *J. Am. Chem. Soc.* **1985**, *107*, 6801.

(6) (a) Schneider, W.; Thiel, W. *Chem. Phys.* **1992**, *159*, 49. (b) Schneider, W.; Thiel, W. *J. Chem. Phys.* **1987**, *86*, 923. (c) Shi, Z.; Boyd, R. J. *J. Am. Chem. Soc.* **1990**, *112*, 6789. (d) Gordon, M. S.; Davis, L. P.; Burggraf, L. W. *Chem. Phys. Lett.* **1989**, *163*, 371. (e) Schmidt, M. W.; Gordon, M. S. *Can. J. Chem.* **1985**, *63*, 1609. (f) Luke, B. T.; Pople, J. A.; Krogh-Jespersen, M.-B.; Apeloig, Y.; Chandrasekhar, J.; Schleyer, P. v. R. *J. Am. Chem. Soc.* **1986**, *108*, 260. (g) Vacek, G.; Mastryukov, V. S.; Schaefer, H. F., III. *J. Phys. Chem.* **1994**, *98*, 11337. (h) Berger, S.; Bock, W.; Frenking, G.; Jonas, V.; Müller, F. *J. Am. Chem. Soc.* **1995**, *117*, 3820. (i) Su, M.-D.; Schlegel, H. B. *J. Phys. Chem.* **1993**, *97*, 8732. (j) Coffey, D., Jr.; Smith, B. J.; Radom, L. J. *Chem. Phys.* **1993**, *98*, 3952. (k) Binning, R. C., Jr.; Curtiss, L. A. *J. Comput. Chem.* **1990**, *11*, 1206. (l) Ochterski, J. W.; Petersson, G. A.; Wiberg, K. B. *J. Am. Chem. Soc.* **1995**, *117*, 11299. (m) Su, M.-D.; Schlegel, H. B. *J. Phys. Chem.* **1993**, *97*, 9981.

0276-7333/96/2315-1477$12.00/0

Scheme 1

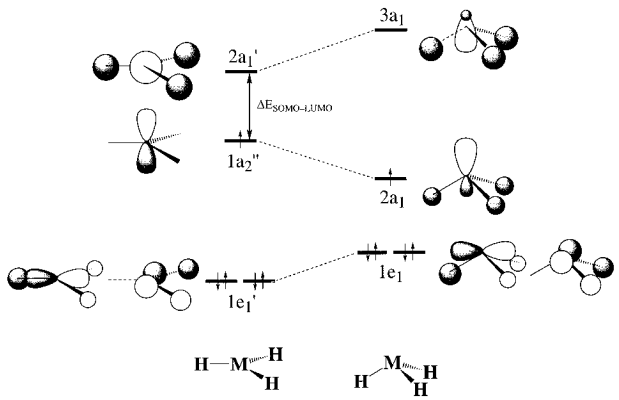

significantly when the central atom M changes from carbon (83.4 kcal/mol) to the heavier silicon (125.5 kcal/mol).[3a]

The $MH_3^•$ radical appears naturally, namely as a building block, in the investigation of the MH_3-X bond. Furthermore, the $MH_3^•$ series displays a trend which is interesting by itself: the degree of pyramidalization as well as the height of the inversion barrier increases when M is running down in group 14, starting with the flat D_{3h} symmetric methyl radical (Chart 1).[7−12] Similar trends are known for the closed-shell group 15 (AH_3) and group 16 hydrides (AH_2)[10−14] as well as for the allylic $CH_2{=}CH{-}MH_2^-$ anions where M is a group 14 atom.[15] This is generally explained in MO theoretical terms through the operation of a second-order Jahn−Teller effect (Scheme 1):[11,13] (1) the mixing between the nonbonding np_z SOMO and the M−H antibonding LUMO stabilizes and pyramidalizes $MH_3^•$; (2) this effect becomes stronger for the heavier (more electropositive and diffuse) central atoms M, because the SOMO−LUMO gap becomes smaller due to the higher energy of the np_z SOMO and the less M−H antibonding nature of the LUMO; (3) the Jahn−Teller effect is opposed by the rising energy of the $1e_1$ orbitals which is ascribed to the loss of M−H bonding overlap; (4) thus, only $CH_3^•$ remains planar because the Jahn−Teller effect is not strong enough in this case to outweigh the $1e_1$ destabilization. In addition, $MH_3^•$ radicals and the corresponding cations play an important role as reactive intermediates[1] and are (M = Si, Ge) involved in processes (e.g. chemical vapor deposition, CVD) which are important for the production of high-technology electronic devices.[16]

In the present study, we have carried out a high-level density functional theoretical (DFT)[17,18] investigation on MH_3Cl and $MH_3^•$ systems for M = C, Si, Ge, and Sn, using the ADF program.[19,20] The purpose is to better understand the structural and bonding trends along the MH_3Cl and $MH_3^•$ series. Why, for example, does the MH_3-Cl bond strength increase in going from CH_3Cl to SiH_3Cl and then decrease for heavier homologs as will be shown? What in this trend is the role of intraatomic Pauli repulsion?[21] The latter is a way to view the effect of the Pauli exclusion principle which is responsible for the existence of (core) electron shells and, thus, for the increasing effective size of atoms, going down the periodic table.[21] The present results for

(7) (a) Yamada, C.; Hirota, E.; Kawaguchi, K. *J. Chem. Phys.* **1981**, *75*, 5256. (b) Yamada, C.; Hirota, E. *Phys. Rev. Lett.* **1986**, *56*, 923. (c) Jackel, G. S.; Gordy, W. *Phys. Rev.* **1968**, *176*, 443. (d) Jackel, G. S.; Christiansen, J. J.; Gordy, W. *J. Chem. Phys.* **1967**, *47*, 4274. (e) The ESR geometries are deduced from the average s character of the three bonding orbitals: 33, 29, 30, and 31% for $CH_3^•$, $SiH_3^•$, $GeH_3^•$, and $SnH_3^•$; our corresponding NL-SCF/TZ2P values are 33, 31, 31, and 30%. (f) Johnson, R. D., III; Tsai, B. P.; Hudgens, J. W. *J. Chem. Phys.* **1988**, *89*, 4558.

(8) (a) Selmani, A.; Salahub, D. R. *Chem. Phys. Lett.* **1988**, *146*, 465. (b) Moc, J.; Rudzinski, J. M.; Ratajczak, H. *Chem. Phys.* **1992**, *109*, 197. (c) Chatgilialoglu, C.; Guerra, M. *J. Am. Chem. Soc.* **1990**, *112*, 2854. (d) Trinquier, G. *J. Chem. Soc., Faraday Trans.* **1993**, *89*, 775. (e) Michels, H. H.; Hobbs, R. H. *Chem. Phys. Lett.* **1993**, *207*, 389. (f) Guerra, M. *J. Am. Chem. Soc.* **1993**, *115*, 11926. (g) Moc, J.; Rudzinski, J. M.; Ratajczak, H. *Z. Phys. D* **1992**, *22*, 629.

(9) (a) Cremer, D.; Olsson, L.; Ottosson, H. *J. Mol. Struct. (THEOCHEM)* **1994**, *313*, 91. (b) Nyalászi, L.; Belghazi, A.; Szétsi, S. K.; Veszprémi, T.; Heinicke, J. *J. Mol. Struct. (THEOCHEM)* **1994**, *313*, 73. (c) Rodriquez, C. F.; Hopkinson, A. C. *Can. J. Chem.* **1992**, *70*, 2234. (d) Das, K. K.; Balasubramanian, K. *J. Chem. Phys.* **1990**, *93*, 5883. (e) Green, W. H.; Jayatilaka, D.; Willetts, A.; Amos, R. D.; Handy, N. C. *J. Chem. Phys.* **1990**, *93*, 4965. (f) Allen, W. D.; Schaefer, H. F., III. *Chem. Phys.* **1986**, *108*, 243.

(10) (a) Binning, R. C., Jr.; Curtiss, L. A. *J. Chem. Phys.* **1990**, *92*, 3688. (b) Binning, R. C., Jr.; Curtiss, L. A. *J. Chem. Phys.* **1990**, *92*, 1860. (c) Pople, J. A.; Curtiss, L. A. *J. Phys. Chem.* **1987**, *91*, 155. (d) Pople, J. A.; Luke, B. T.; Frisch, M. J.; Binkley, J. S. *J. Phys. Chem.* **1985**, *89*, 2198. (e) Marynick, D. S. *J. Chem. Phys.* **1981**, *74*, 5186.

(11) (a) Albright, T. A.; Burdett, J. K.; Whangbo, M.-H. *Orbital Interactions in Chemistry;* Wiley-Interscience: New York, 1985; Chapters 7 and 9. (b) Gimarc, B. M. *Molecular Structure and Bonding*; Academic Press: New York, 1979; Chapter 3.

(12) Gillespie, R. J.; Hargittai, I. *The VSEPR Model of Molecular Geometry*; Allyn and Bacon: Boston, MA, 1991.

(13) Gilheany, D. G. *Chem. Rev.* **1994**, *94*, 1339.

(14) (a) Dixon, D. A.; Arduengo, A. J., III. *J. Am. Chem. Soc.* **1987**, *109*, 338. (b) Reed, A. E.; Schleyer, P. v. R. *J. Am. Chem. Soc.* **1987**, *109*, 7362. (c) Magnusson, E. *Tetrahedron* **1985**, *41*, 5235. (d) *Ibid.* **1985**, *41*, 2945. (e) Magnusson, E. *J. Am. Chem. Soc.* **1984**, *106*, 1185. (f) Magnusson, E. *J. Am. Chem. Soc.* **1984**, *106*, 1177. (g) Hall, M. B. *J. Am. Chem. Soc.* **1978**, *100*, 6332.

(15) Gobbi, A.; Frenking, G. *J. Am. Chem. Soc.* **1994**, *116*, 9287.

(16) See for some examples the following references: (a) Gal, J.-F.; Grover, R.; Maria, P.-C.; Operti, L.; Rabezzana, R.; Vaglio, G.-A.; Volpe, P. *J. Phys. Chem.* **1994**, *98*, 11978. (b) Davies, P. B.; Smith, D. M. *J. Chem. Phys.* **1994**, *100*, 6166. (c) Lu, G.; Crowell, J. E. *J. Chem. Phys.* **1993**, *98*, 3415. (d) Operti, L.; Splendore, M.; Vaglio, G. A.; Volpe, P. *Organometallics* **1993**, *12*, 4516. (e) Schleyer, P. v. R.; Buzek, P.; Müller, T.; Apeloig, Y.; Siehl, H.-U. *Angew. Chem.* **1993**, *105*, 1558. (f) Ruscic, B.; Schwarz, M.; Berkowitz, J. *J. Chem. Phys.* **1990**, *92*, 1865. Erratum: *Ibid.* **1990**, *92*, 6338. (g) Raghavachari, K. *J. Chem. Phys.* **1990**, *92*, 452.

(17) (a) Dreizler, R. M.; Gross, E. K. U. *Density Functional Theory, An Approach to the Quantum Many-Body Problem;* Springer-Verlag: Berlin, 1990. (b) Parr, R. G.; Yang, W. *Density-Functional Theory of Atoms and Molecules*; Oxford University Press: New York, 1989. (c) Slater, J. C. *Quantum Theory of Molecules and Solids*; McGraw-Hill: New York, 1974; Vol. 4.

(18) (a) Ziegler, T. *Chem. Rev.* **1991**, *91*, 651. (b) *Density Functional Methods in Chemistry*; Labanowski, J. K., Andzelm, J. W., Eds.; Springer-Verlag: New York, 1991.

(19) (a) Baerends, E. J.; Ellis, D. E.; Ros, P. *Chem. Phys.* **1973**, *2*, 41. (b) Baerends, E. J.; Ros, P. *Chem. Phys.* **1975**, *8*, 412. (c) Baerends, E. J.; Ros, P. *Int. J. Quantum Chem., Quantum Chem. Symp.* **1978**, *S12*, 169. (d) Ravenek, W. In *Algorithms and Applications on Vector and Parallel Computers*; Riele, H. H. J., Dekker, Th. J., van de Vorst, H. A., Eds.; Elsevier: Amsterdam, 1987. (e) Boerrigter, P. M.; te Velde, G.; Baerends, E. J. *Int. J. Quantum Chem.* **1988**, *33*, 87. (f) te Velde, G.; Baerends, E. J. *J. Comp. Phys.* **1992**, *99*, 84. (g) Snijders, J. G.; Baerends, E. J.; Vernooijs, P. *At. Nucl. Data Tables* **1982**, *26*, 483. (h) Krijn, J.; Baerends, E. J. Fit-Functions in the HFS-Method, Internal Report (in Dutch), Vrije Universiteit Amsterdam, The Netherlands, 1984. (i) Baker, J.; Nobes, R. H.; Radom, L. *J. Comput. Chem.* **1986**, *7*, 349. (j) Gutsev, G. L.; Ziegler, T. *J. Phys. Chem.* **1991**, *95*, 7220. (k) Gutsev, G. L.; Ziegler, T. *Can. J. Chem.* **1991**, *69*, 993. (l) Versluis, L.; Ziegler, T. *J. Chem. Phys.* **1988**, *88*, 322. (m) Fan, L.; Versluis, L.; Ziegler, T.; Baerends, E. J.; Ravenek, W. *Int. J. Quantum Chem., Quantum Chem. Symp.* **1988**, *S22*, 173. (n) Vosko, S. H.; Wilk, L.; Nusair, M. *Can. J. Phys.* **1980**, *58*, 1200. (o) Becke, A. D. *J. Chem. Phys.* **1986**, *84*, 4524. (p) Becke, A. D. *Phys. Rev. A* **1988**, *38*, 3098. (q) Perdew, J. P. *Phys. Rev. B* **1986**, *33*, 8822. Erratum: *Ibid.* **1986**, *34*, 7406. (r) Fan, L.; Ziegler, T. *J. Chem. Phys.* **1991**, *94*, 6057.

(20) (a) Bickelhaupt, F. M.; Nibbering, N. M. M.; van Wezenbeek, E. M.; Baerends, E. J. *J. Phys. Chem.* **1992**, *96*, 4864. (b) Ziegler, T.; Rauk, A. *Inorg. Chem.* **1979**, *18*, 1558. (c) Ziegler, T.; Rauk, A. *Inorg. Chem.* **1979**, *18*, 1755. (d) Ziegler, T.; Rauk, A. *Theoret. Chim. Acta* **1977**, *46*, 1.

(21) (a) Jacobsen, H.; Ziegler, T. *J. Am. Chem. Soc.* **1994**, *116*, 3667. (b) Kutzelnigg, W. *Angew. Chem.* **1984**, *96*, 262.

MH_3Cl are compared with those obtained previously for the CH_3X series (X = F, Cl, Br, I).[5a] Furthermore, it is discussed how the electronic structure varies in the different MH_3X systems and how this may influence their reactivity in S_N2 reactions; e.g. why is the backside lobe of the chloromethane LUMO so poorly developed, as has been pointed out recently?[22] First, however, we focus on the $MH_3^{\bullet}$ building block and the question why the degree of pyramidalization increases along M = C, Si, Ge and Sn. Is this to be conceived as a purely "electronic" effect or does steric repulsion also play a role? Detailed analyses[20] of the electronic structures and bonding mechanisms in all MH_3Cl and $MH_3^{\bullet}$ systems enable us to interpret our results in chemically meaningful terms from MO theory[11,23] and, thus, help to answer the above and other questions.

2. Methods

A. General Procedure. All calculations were performed using the Amsterdam-Density-Functional (ADF) program,[19] developed by Baerends *et al.*[19a−c] and vectorized by Ravenek.[19d] The numerical integration was performed using the procedure developed by te Velde *et al.*[19e,f] The MOs were expanded in a large uncontracted set of Slater type orbitals (STOs) containing diffuse functions (TZ2P).[19g] The basis set is of triple-ζ quality, augmented with two polarization functions: three 2p on H, two 3d functions on C, Si, and Cl, 3d and 4f on F, two 4d on Ge, and two 5d on Sn (ζ_{1s}^{H} = 0.69, 0.92, 1.58; ζ_{2p}^{H} = 2.50, 1.66, 1.10; ζ_{2s}^{C} = 1.28, 2.10, 4.60; ζ_{2p}^{C} = 0.82, 1.48, 2.94; ζ_{3d}^{C} = 3.00, 1.50; ζ_{2s}^{F} = 0.74, 1.94, 3.24; ζ_{2p}^{F} = 1.24, 2.30, 4.54; ζ_{3d}^{F} = 2.00; ζ_{4f}^{F} = 3.00; ζ_{3s}^{Si} = 1.20, 1.85, 2.85; ζ_{3p}^{Si} = 0.75, 1.20, 1.85; ζ_{3d}^{Si} = 0.65, 1.75; ζ_{3s}^{Cl} = 1.60, 2.30, 3.30; ζ_{3p}^{Cl} = 1.20, 2.05, 2.85; ζ_{3d}^{Cl} = 1.20, 2.20; ζ_{3d}^{Ge} = 2.50, 4.80, 9.20; ζ_{4s}^{Ge} = 1.25, 1.95, 3.15; ζ_{4p}^{Ge} = 0.80, 1.35, 2.35; ζ_{4d}^{Ge} = 0.80, 2.00; ζ_{4d}^{Sn} = 2.30, 3.70, 5.65; ζ_{5s}^{Sn} = 1.35, 2.10, 3.25; ζ_{5p}^{Sn} = 0.90, 1.45, 2.45; ζ_{5d}^{Sn} = 1.90, 0.90). The core shells of carbon and fluorine (1s), silicon and chlorine (1s2s2p), germanium (1s2s2p3s3p), and tin (1s2s2p3s3p3d4s4p) were treated by the frozen-core approximation.[19a] An auxiliary set of s, p, d, f, and g STOs was used to fit the molecular density and to represent the Coulomb and exchange potentials accurately in each SCF cycle.[19h] Our TZ2P basis is of the composition recommended by Baker *et al.*[19i] for negative ions and has been successfully applied to the calculation of electron affinities of, i.a., CX^-, CXY^-, and CCl_n^- ($n = 1-4$);[19j,k] this flexibility is of importance for the analysis of the CH_3Cl and CH_3F LUMOs in section 3E.

Geometries were calculated at the LDA and NL level. Equilibrium structures were optimized using analytical gradient techniques.[19l] Frequencies[19m] were calculated at the LDA level by numerical differentiation of the analytical energy gradients.

Energies were evaluated using the local density approximation (LDA) as well as density-functionals including nonlocal corrections (NL). At the LDA level exchange is described by Slaters Xα potential[17c] and correlation is treated in the Vosko−Wilk−Nusair (VWN) parametrization.[19n] At the NL-SCF level nonlocal corrections for the exchange due to Becke[19o,p] and for correlation due to Perdew[19q] are added self-consistently (NL-SCF).[19r]

B. Bonding Energy Analysis. The bonding mechanism in the various $MH_3^{\bullet}$ and MH_3Cl systems was analyzed using an extended transition state (ETS) method developed by Ziegler and Rauk.[20] This was done at the NL-P level (nonlocal corrections added as a perturbation to the LDA result) for technical reasons. The NL-P analysis results are scaled to fit the bond energies with the corresponding NL-SCF values (which differ consistently by a few kcal/mol) to facilitate a straightforward comparison. The overall bond energy ΔE is made up of two major components (eq 1). The preparation

$$\Delta E = \Delta E_{prep} + \Delta E_{int} \quad (1)$$

energy ΔE_{prep} is the amount of energy required to deform the separated fragments from their equilibrium structure to the geometry which they acquire in the overall molecule. The interaction energy ΔE_{int} corresponds to the actual energy change when the prepared fragments are combined to form the overall molecule. The interaction energy is further split up in two physically meaningful terms (eq 2).[20] The term ΔE_{elst}

$$\Delta E_{int} = \Delta E_{elst} + \Delta E_{Pauli} + \Delta E_{oi} = \Delta E^0 + \Delta E_{oi} \quad (2)$$

corresponds to the classical electrostatic interaction between the unperturbed charge distributions of the prepared fragments and is usually attractive. The Pauli-repulsion ΔE_{Pauli} comprises the 4-electron destabilizing interactions between occupied orbitals and is responsible for the steric repulsion. For neutral fragments, it is useful to combine ΔE_{elst} and ΔE_{Pauli} in the steric interaction ΔE^0 (eq 2). The orbital interaction ΔE_{oi} accounts for charge transfer (interaction between occupied orbitals on one moiety with unoccupied orbitals of the other, including the HOMO−LUMO interactions) and polarization (empty/occupied orbital mixing on one fragment). It can be decomposed into the contributions from each irreducible representation Γ of the interacting system (eq 3).

$$\Delta E_{oi} = \sum_{\Gamma} \Delta E_{\Gamma} \quad (3)$$

3. Results and Discussion

The results are summarized in Tables 1 and 2 (geometries), 3 and 4 (MH_3 energies), and 5 and 6 (MH_3-Cl energies). In the following, the trends in $MH_3^{\bullet}$ geometries and inversion barriers are discussed (section 3A); we try to explain these trends through a detailed analysis of the bonding mechanisms (section 3B). Thereafter, the MH_3Cl geometries and M−Cl bond dissociation energies are presented (section 3C) and analyzed (section 3D). Finally, the nature of the MH_3X LUMO is considered in more detail (section 3E).

Geometries (Table 1) and energies (Tables 3 and 5) were evaluated at the LDA/TZ2P and NL-SCF/TZ2P levels. At the LDA level, the M−Cl bonds are up to 0.03 Å shorter than at the NL-SCF level (Table 1). The $MH_3^{\bullet}$ inversion barriers are ca. 1 kcal/mol lower (Table 3) and M−Cl bonds are up to 20 kcal/mol stronger (Table 5) at the LDA/TZ2P than at the NL-SCF/TZ2P level, in agreement with the general tendency of LDA to overestimate bond strengths and to underestimate transition state barriers. The discussion is therefore based on the nonlocal results.

A. $MH_3^{\bullet}$ Geometry and Inversion Barrier. The $CH_3^{\bullet}$ radical is planar (D_{3h}) whereas the heavier central atom analogs are pyramidal: the H−M−H bond angle β (=120.00, 112.66, 112.44, 110.56°) decreases and the inversion barrier corrected for zero point vibrational energy effects ΔE_{inv} + ΔZPE (=0.0, 3.7, 3.8, 7.0 kcal/mol) increases monotonically along the series $CH_3^{\bullet}$, $SiH_3^{\bullet}$, $GeH_3^{\bullet}$, and $SnH_3^{\bullet}$ (Tables 1 and 3, NL-SCF/TZ2P). Note, however, that $SiH_3^{\bullet}$ and $GeH_3^{\bullet}$ have essentially the same degree of pyramidalization and that the inversion barrier of $GeH_3^{\bullet}$ is slightly higher only after correction for ΔZPE. Furthermore, the equilibrium

(22) Bickelhaupt, F. M.; Ziegler, T.; Schleyer, P. v.R. *Organometallics* **1995**, *14*, 2288.
(23) Rauk, A. *Orbital Interaction Theory of Organic Chemistry*; Wiley-Interscience: New York, 1994.

Table 1. Optimized Geometries of $MH_3^•$, MH_3^+, and MH_3Cl (in Å, deg)[a]

		LDA/TZ2P				NL-SCF/TZ2P			
system	NIMAG[b]	d_{MCl}	d_{MH}	α	β	d_{MCl}	d_{MH}	α	β
planar MH_3^+ [c]									
CH_3^+	0		1.106	90	120		1.102	90	120
SiH_3^+	0		1.463	90	120		1.459	90	120
GeH_3^+	0		1.485	90	120		1.491	90	120
SnH_3^+	0		1.721	90	120		1.746	90	120
planar $MH_3^•$ [c]									
$CH_3^•$-plan	0		1.089	90	120		1.088	90	120
$SiH_3^•$-plan	1 (*i*610.9)[d]		1.471	90	120		1.470	90	120
$GeH_3^•$-plan	1 (*i*554.8)[d]		1.493	90	120		1.505	90	120
$SnH_3^•$-plan	1 (*i*436.5)[d]		1.711	90	120		1.733	90	120
pyramidal $MH_3^•$ [e]									
$CH_3^•$-pyr[f]	*f*		1.097[f]	107.67[f]	111.21[f]		1.094[f]	106.06[f]	112.66[f]
$SiH_3^•$-pyr	0		1.488	107.67	111.21		1.484	106.06	112.66
$GeH_3^•$-pyr	0		1.516	107.13	111.71		1.524	106.31	112.44
$SnH_3^•$-pyr	0		1.738	108.71	110.22		1.755	108.36	110.56
MH_3Cl									
CH_3Cl	0	1.753	1.096	109.30	109.64	1.779	1.094	108.40	110.52
SiH_3Cl	0	2.017	1.482	109.14	109.80	2.034	1.479	108.63	110.30
GeH_3Cl	0	2.104	1.511	107.60	111.28	2.129	1.518	107.23	111.62
SnH_3Cl	0	2.333	1.733	106.41	112.35	2.361	1.744	106.36	112.40

[a] See Scheme 1 for definition of geometry parameters. [b] Number of imaginary frequencies (LDA/TZ2P). [c] Optimized in D_{3h} symmetry. [d] Imaginary frequency (in cm^{-1}) corresponding to A_2'' inversion of $MH_3^•$. [e] Optimized in C_{3v} symmetry. [f] d_{MH} optimized in C_{3v} symmetry with fixed α from $SiH_3^•$-pyr C_{3v} optimization.

M−H bond length increases from 1.088 Å in $CH_3^•$-plan to 1.755 Å in $SnH_3^•$-pyr (Table 1). The transition states for inversion ($MH_3^•$-plan) are characterized by one imaginary frequency (=*i*610.9, *i*554.8, and *i*436.5 cm^{-1}) which decreases along $SiH_3^•$, $GeH_3^•$, and $SnH_3^•$ (Table 1); the potential energy surface is thus becoming still shallower. The planar transition states display a slight M−H contraction of 0.01−0.02 Å with respect to the pyramidal equilibrium structures. For comparison, the corresponding MH_3^+ cations are planar for each M.

Our results agree well with most of the available literature data (Tables 2 and 3).[7−10] At the Hartree−Fock level,[8b,10d] the H−M−H angle β (=120, 110.9, 110.7, and 109.3°; Table 2) decreases again along $CH_3^•$, $SiH_3^•$, $GeH_3^•$, and $SnH_3^•$, but it is slightly more pyramidal than ours at NL-SCF/TZ2P. Similar results were also obtained at the LSD level,[8a] but here $SiH_3^•$ (β = 111.6°) is slightly more pyramidal than $GeH_3^•$ (β = 113°). The most accurate *ab initio* studies available (CISD and CASSCF) yield again an $SiH_3^•$ (β = 111.1 or 112.6°)[9f,10e] which is less pyramidal than $GeH_3^•$ (β = 110.7°).[9d] Apparently, the precise order for these two $MH_3^•$ radicals depends delicately on the level of theory. Experiments confirm that $CH_3^•$ is planar and that the heavier homologs are pyramidal (Table 2).[7] There seems to be a slight discrepancy with ESR experiments which indicate a continuous decrease of pyramidalization (β = 114, 115, and 117°) along $SiH_3^•$, $GeH_3^•$, and $SnH_3^•$.[7c,e] This may tentatively be ascribed to slightly different matrix effects on the ESR spectra of different $MH_3^•$ radicals.

Our NL-SCF/TZ2P trend in inversion barriers ΔE_{inv} (without ΔZPE!) agrees satisfactorily with the trends obtained at LSD-LCGTO[8a] and UHF/3-21G*[8b] (Table 3); barriers are however underestimated by the former and overestimated by the latter. The agreement with higher level *ab initio* results for $SiH_3^•$ (4.4 at NL-SCF *versus* 5.8 or 4.4 kcal/mol at CISD)[9f,10e] and $GeH_3^•$ (4.3 at NL-SCF *versus* 4.6 kcal/mol at CASSCF)[9d] is excellent (Table 3).

B. $MH_3^•$ Bonding Mechanism. In this section, we try to *understand* the trends in pyramidalization and inversion barrier of the four $MH_3^•$ radicals, through detailed analyses of the M−H bonding and the H−H repulsive interactions (see also section 2B). The overall bond energy ΔE is divided into three components (eq 4,

$$M + 3H^• \rightarrow MH_3^•$$
$$\Delta E = \Delta E_{int}(M{-}H_3) + \Delta E_{int}(H_3) + \Delta E(M\text{-}sp^3) \quad (4)$$

Table 4). The promotion energy $\Delta E(M\text{-}sp^3)$ is the amount of energy required to bring the group-14 atom M from its s^2p^2 ground state to its valence sp^3 configuration (eq 5). The interaction energy $\Delta E_{int}(H_3)$ corresponds to the formation of the $(H^•)_3$ triangle in its quartet valence configuration and in the geometry which it acquires in the overall molecule (eq 6). Finally, the interaction energy $\Delta E_{int}(M{-}H_3)$ corresponds to the actual energy change when the prepared M-sp^3 and $(H^•)_3$ fragments are combined to form the M−H bond (eq 7).

$$M \rightarrow M\text{-}sp^3 \qquad \Delta E(M\text{-}sp^3) \quad (5)$$

$$3H^• \rightarrow (H^•)_3 \qquad \Delta E_{int}(H_3) = \Delta E^0(H_3) + \Delta E_{oi}(H_3) \quad (6)$$

$$M\text{-}sp^3 + (H^•)_3 \rightarrow (H^•)_3$$
$$\Delta E_{int}(M{-}H_3) = \Delta E^0(M{-}H_3) + \Delta E_{oi}(M{-}H_3) \quad (7)$$

Electronic Structure and Orbital Interactions. How are the various energy terms related to the electronic structure and the orbital interactions? First, we consider the formation of the quartet $(H^•)_3$ fragment (Scheme 2):[24] the three same-spin, singly occupied hydrogen 1s AOs enter into a 3-orbital−3-electron interaction which yields a bonding $1a_1'$ and a degenerate pair of antibonding $1e_1'$ orbitals, each occupied by one β-electron. This gives primarily rise to steric repulsion

(24) See also ref 11a, Chapter 5.2, and ref 11b, Chapter 2.

Table 2. Literature Values for the Geometries of $MH_3^{\bullet}$, MH_3^+, and MH_3Cl (in Å, deg)[a]

system	d_{MCl}	d_{MH}	α	β	method	ref
planar MH_3^+						
CH_3^+		1.078		120	HF/6-31G(d)	9a, 10c
SiH_3^+		1.451		120	MP2/TZ2P+f	9e
		1.454		120	HF/6-31G(d)	9a, 10c
GeH_3^+		1.517		120	HF/641(d)	10a
		1.509		120	CASSCF/MRSDCI	9d
planar $MH_3^{\bullet}$						
$CH_3^{\bullet}$-plan		1.10		120	LSD-LCGTO	8a
		1.073		120	HF/6-31G(d)	10d
		1.082		120	HF/DZP	8d
		1.079		120	EXP IR	7a
				120	EXP ESR	7c
$SiH_3^{\bullet}$-plan		1.462		120	UHF/3-21G*	8b
		1.470		120	MP2/6-31G*	9b
$GeH_3^{\bullet}$-plan		1.528		120	UHF/3-21G*	8b
		1.500		120	UMP2/BAS2	8g
$SnH_3^{\bullet}$-plan		1.726		120	UHF/3-21G*	8b
pyramidal $MH_3^{\bullet}$						
$SiH_3^{\bullet}$-pyr		1.50		111.6	LSD-LCGTO	8a
		1.475		110.9	UHF/3-21G*	8b
		1.474		111.1	HF/DZP	8d
		1.4830		111.255	MP2/6-31G*	8e
		1.4766		111.15	UMP2/DZP	8f
		1.473		111.2	MP2(full)/6-31G*	6i
		1.477		111.1	CISD/CGF-TZ2P	9f
		1.488		112.6	CISD/STO-DZP	10e
		1.476		111.0	HF/6-31++G(d,p)	9c
		1.476		110.9	HF/6-31G(d)	10d
		1.483		107.63	MP2/6-31G*	9b
		1.468[b]		110.5[b]	EXP IR[b]	7b
		1.456[b]		108.5[b]	EXP IR[b]	7b
				114	EXP ESR	7c
$GeH_3^{\bullet}$-pyr		1.535		113	LSD-LCGTO	8a
		1.549		110.7	UHF/3-21G*	8b
		1.549		110.7	HF/DZP	8d
		1.519		111.6	UMP2/BAS2	8g
		1.539		110.8	HF/641(d)	10b
		1.526		110.7	CASSCF/MRSDCI	9d
				115	EXP ESR	7d
$SnH_3^{\bullet}$-pyr		1.69		112	LSD-LCGTO	8a
		1.750		109.3	UHF/3-21G*	8b
		1.717		109.4	HF/DZP	8d
				117	EXP ESR	7d
MH_3Cl						
CH_3Cl	1.777	1.078	108.5	110.5	HF/ECP1*	6b
	1.779	1.089	108.9		MP2/6-31++G**	6c
	1.784	1.082	108.2		HF/3-21G+d	6e
	1.787	1.088	108.7		MP2/6-311+G**	6j
	1.782	1.087	108.8		CISD/6-31G*	6j
	1.787	1.091	108.8		CISD(Q)/6-31G*	6j
	1.778	1.086	108.2	110.7	EXP MW	2c
	1.785	1.090		110.8	EXP MW, IR	2d
SiH_3Cl	2.042	1.452	108.6	110.4	HF/ECP1*	6b
	2.058	1.479	108.63		MP2/6-31G*	9b
	2.056	1.468	108.6	110.3	MP2(full)/6-31G*	6i
	2.051	1.465	108.4		HF/3-21G+d	6e
	2.067	1.468	108.3		HF/6-31G(d)	6d
	2.048	1.482	107.9	111.0	EXP MW	2c
	2.048	1.481	108.0		EXP MW, IR	2d
GeH_3Cl	2.155	1.527	107.5	111.4	HF/ECP1*	6b
	2.174	1.530	107.0		HF/641(d)	6k
	2.149	1.520	105.6	113.0	EXP MW/IR	2b
	2.150	1.537		111.0	EXP MW, IR	2d
SnH_3Cl	2.336	1.702	106.7	112.1	HF/ECP1*	6b
	2.328	1.696[c]	105.5[c]	113.1[c]	EXP FT-IR[c]	2a

[a] See Scheme 1 for definition of geometry parameters. [b] Inferred using two assumed forms of potential function. [c] Geometry of the SnH_3 group was estimated.

$\Delta E^0(H_3)$ which is however counteracted by a stabilizing interaction $\Delta E_{oi}(H_3)$ with hydrogen 2s and 2p AOs.

Next, we inspect the orbital interactions between M-sp^3 and $(H^{\bullet})_3$. In planar $MH_3^{\bullet}$, three (polar) electron pair bonds are formed ($ns \pm 1a_1'$ and $np_{x,y} \pm 1e_1'$); the M-np_z AO becomes, essentially unchanged, the $MH_3^{\bullet}$ $1a_2''$ SOMO, because it has no overlap with $(H^{\bullet})_3$ valence orbitals (Figure 1, left). The corresponding orbital interactions are $\Delta E_A(M-H_3)$ (mainly $ns \pm 1a_1'$) and $\Delta E_E(M-H_3)$ ($np_{x,y} \pm 1e_1'$). In *pyramidal* $MH_3^{\bullet}$, M-np_z *has* overlap and mixes in a bonding fashion with $(H^{\bullet})_3$-$1a_1'$ (Figure 1, right) which yields an additional stabilization

Table 3. Calculated Inversion Barriers ΔE_{inv} of $MH_3^\bullet$ Radicals (in kcal/mol)

	LDA/TZ2P			NL-SCF/TZ2P		literature	
$MH_3^\bullet$	ΔE_{inv}	ΔZPE	$\Delta E_{inv}+\Delta$ZPE	ΔE_{inv}	$\Delta E_{inv}+\Delta$ZPE[a]	theoretical	exptl
$CH_3^\bullet$	0.0	0.0	0.0	0.0	0.0	0.0[b,c]	0.0[d]
$SiH_3^\bullet$	4.0	−0.7	3.3	4.4	3.7	3.0,[b] 4.4,[c] 7.6,[e] 5.8,[f] 4.4,[g] 4.2[h]	5.3,[i] 5.0[i]
$GeH_3^\bullet$	3.7	−0.5	3.2	4.3	3.8	2.7,[b] 7.5,[e] 7.7,[j] 4.6,[k] 4.9,[l] 4.5[m]	4.4[n]
$SnH_3^\bullet$	4.6	1.2	5.8	5.8	7.0	3.0,[b] 10.2[e]	

[a] ΔZPE from LDA/TZ2P frequencies. [b] LSD-LCGTO: ref 8a. [c] MP4/6-31G*//HF/6-31G* + ΔZPE: ref 6f. [d] IR: ref 7a. [e] UHF/3-21G*: ref 8b. [f] CISD/CGF-TZ2P: ref 9f. [g] CISD/STO-DZP+TZP//CISD/STO-DZP: ref 10e. [h] MP2/6-31G*: ref 9b. [i] IR (inferred using two assumed forms of potential function): ref 7b. [j] UHF/6-31G*: ref 8b. [k] CASSCF/MRSDCI: ref 9d. [l] UMP2/BAS2: ref 8g. [m] UMP4SDTQ/BAS4//UMP2/BAS2: ref 8g. [n] REMPI: ref 7f.

Table 4. Analysis of the Bonding Mechanism in Planar and Pyramidal $MH_3^\bullet$ Radicals[a,b]

	$CH_3^\bullet$			$SiH_3^\bullet$			$GeH_3^\bullet$			$SnH_3^\bullet$		
	plan	pyr*[c]	pyr[c]	plan	pyr*	pyr	plan	pyr*	pyr	plan	pyr*	pyr
					Geometry (in Å, deg)							
d_{MH}	1.088	1.088	1.094	1.470	1.470	1.484	1.505	1.505	1.524	1.733	1.733	1.755
α	90.00	106.06	106.06	90.00	106.06	106.06	90.00	106.31	106.31	90.00	108.36	108.36
					Energy (in kcal/mol)[d]							
$\Delta E^0(M-H_3)$	−89.3	−87.0	−88.9	−86.3	−85.0	−87.1	−88.8	−87.0	−89.4	−78.1	−76.5	−78.1
$\Delta E_A(M-H_3)$	−91.5	−94.4	−94.5	−71.5	−76.0	−76.1	−79.1	−84.5	−84.8	−65.5	−72.7	−72.9
$\Delta E_E(M-H_3)$	−252.0	−251.0	−248.5	−167.2	−169.3	−167.0	−160.0	−161.1	−158.7	−137.7	−138.4	−136.5
$\Delta E_{int}(M-H_3)$	−432.8	−432.4	−431.9	−325.0	−330.3	−330.2	−327.9	−332.6	−332.9	−281.3	−287.6	−287.5
$\Delta E^0(H_3)$	24.8	30.2	29.4	4.4	5.7	5.4	3.8	4.9	4.5	1.5	2.1	1.9
$\Delta E_{oi}(H_3)$	−8.5	−9.9	−9.7	−4.1	−4.3	−4.3	−4.1	−4.2	−4.1	−3.9	−3.9	−3.9
$\Delta E(M-sp^3)$	96.9	96.9	96.9	99.4	99.4	99.4	123.2	123.2	123.2	99.7	99.7	99.7
ΔE	−319.6	−315.2	−315.3	−225.3	−229.5	−229.7	−205.0	−208.7	−209.3	−184.0	−189.7	−189.8
					Fragment Orbital Overlaps[e,f]							
H + H $\langle 1s\|1s\rangle$	0.32	0.34	0.34	0.16	0.18	0.18	0.15	0.17	0.17	0.10	0.12	0.11
M + H_3 $\langle ns\|1a_1'\rangle$	0.83	0.82	0.82	0.77	0.76	0.75	0.74	0.73	0.72	0.70	0.68	0.68
M + H_3 $\langle np_z\|1a_1'\rangle$	0.0	0.21	0.21	0.0	0.24	0.24	0.0	0.24	0.24	0.0	0.28	0.28
M + H_3 $\langle np_x\|1e_{1-x}'\rangle$	0.74	0.72	0.72	0.76	0.74	0.74	0.76	0.74	0.73	0.72	0.69	0.68
					Fragment Orbital Populations (in e)[f,g]							
M: $P(ns)$	1.27	1.32	1.33	1.18	1.20	1.22	1.21	1.26	1.28	1.23	1.33	1.35
M: $P(np_z)$	0.93	0.88	0.88	0.95	0.84	0.83	0.94	0.81	0.81	0.95	0.76	0.75
M: $P(np_x)$	0.99	1.08	1.08	1.04	1.06	1.04	0.97	1.00	0.99	0.76	0.79	0.78
H_3: $P(1a_1')$	0.72	0.72	0.72	0.82	0.91	0.90	0.79	0.88	0.87	0.77	0.88	0.87
H_3: $P(1e_{1-x}')$	0.96	0.85	0.86	0.87	0.85	0.86	0.97	0.94	0.95	1.20	1.17	1.18

[a] NL-P/TZ2P//NL-SCF/TZ2P; ΔE_{int} decomposition scaled to fit NL-SCF/TZ2P value. [b] See eq 8: plan = planar, optimized in D_{3h}; pyr = pyramidal, optimized in C_{3v}; pyr* = pyramidal, d_{MH} from D_{3h} optimization, α from C_{3v} optimization. [c] α from $SiH_3^\bullet$ C_{3v} optimization. [d] See eqs 4−7: $\Delta E^0(M-H_3)$, $\Delta E_{oi}(M-H_3) = \Delta E_A(M-H_3) + \Delta E_E(M-H_3)$, $\Delta E_{int}(M-H_3)$ = steric, orbital, and net interaction between M-sp^3 and H_3 in $MH_3^\bullet$; $\Delta E^0(H_3)$, $\Delta E_{oi}(H_3)$ = steric and orbital interaction between 3 $H^\bullet$ in $(H^\bullet)_3$; $\Delta E(M\text{-}sp^3)$ = $sp-sp^3$ promotion energy; ΔE = overall energy change for M-sp^3 + 3$H^\bullet$ → $MH_3^\bullet$. [e] Overlaps between orbitals of the indicated fragments. [f] n (in ns and np) = 2, 3, 4, and 5 for M = C, Si, Ge, Sn, respectively. [g] $P(\varphi)$ is the gross Mulliken population which fragment orbital φ acquires in the overall molecule.

of $\Delta E_A(M-H_3)$ (Table 4). The Pauli repulsion between M-sp^3 and $(H^\bullet)_3$ is very small because the two fragments have opposite spin; Pauli repulsion can thus only occur through core−valence overlap.

Planar *vs* Pyramidal: Quantitative Trends in Interactions. The H−H and M−H interactions were analyzed for three geometries of each $MH_3^\bullet$ radical (eq 8): (1) $MH_3^\bullet$-plan, the optimized planar structure; (2)

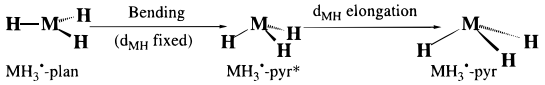

(8)

$MH_3^\bullet$-pyr*, in which d_{MH} is kept fixed to its value in the planar radical, whereas the H−M−H angle β is bent to its value in the optimized pyramidal structure; (3) $MH_3^\bullet$-pyr, the optimized pyramidal structure in which d_{MH} is allowed to elongate to its equilibrium value. Note that for both $CH_3^\bullet$-pyr* and $CH_3^\bullet$-pyr the optimum H−M−H angle β of $SiH_3^\bullet$-pyr was used, because there is no stationary point corresponding to a pyramidal methyl radical (Table 4).

The geometry of $MH_3^\bullet$ is primarily determined by the subtle balance between the H−H steric repulsion ΔE^0-(H_3) (eq 6) and the M−H bonding orbital interactions $\Delta E_{oi}(M-H_3)$ (eq 7). The steric interaction $\Delta E^0(M-H_3)$ is dominated by electrostatic attraction and is relatively insensitive to H−M−H bond angle variations (Table 4). The promotion energy $\Delta E(M\text{-}sp^3)$ has no influence at all on the geometry because, for a given central atom M, it leads to a constant (endothermic) contribution between 97 kcal/mol for C and 123 kcal/mol for Ge (Table 4).

Scheme 2

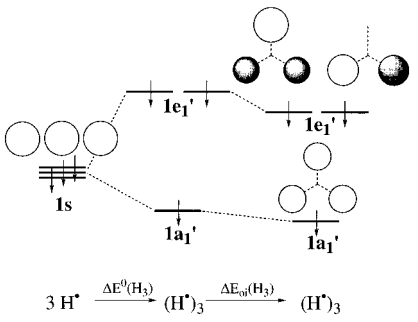

There is a striking difference between $CH_3^\bullet$ and the heavier homologs: in $CH_3^\bullet$, the H−H steric repulsion

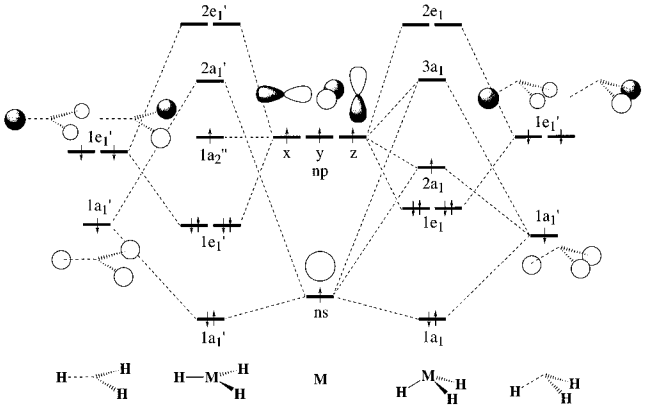

Figure 1. Orbital interaction scheme for planar (D_{3h}) and pyramidal (C_{3v}) $MH_3^{\bullet}$.

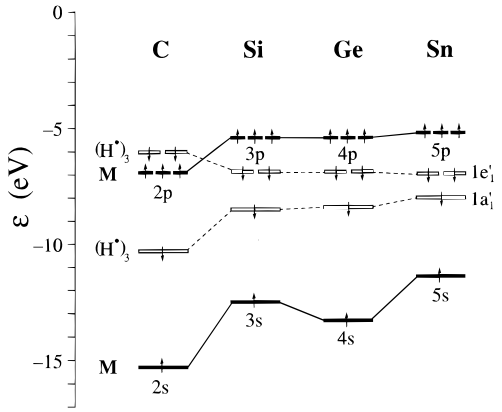

Figure 2. Orbital energies of C, Si, Ge, Sn, and $(H^{\bullet})_3$ (in the geometry of the corresponding $MH_3^{\bullet}$ radical).

$\Delta E^0(H_3)$ is significantly stronger and increases much more upon pyramidalization. This is seen most clearly from a comparison of $MH_3^{\bullet}$-plan and $MH_3^{\bullet}$-pyr*: $\Delta E^0(H_3)$ rises by 5.4 kcal/mol for $CH_3^{\bullet}$ and only by 1.3 kcal/mol or less for $SiH_3^{\bullet}$, $GeH_3^{\bullet}$, and $SnH_3^{\bullet}$ (Table 4). This trend is also reflected by the decreasing $(H^{\bullet})_3$ $1a_1'-1e_1'$ energy gap shown in Figure 2. The reason is the shorter M−H and thus H−H distance in $CH_3^{\bullet}$ and the associated larger H−H $\langle 1s|1s\rangle$ overlap. The H−H repulsion is slightly relieved (and thus partly hidden) after the M−H bond is allowed to elongate in $MH_3^{\bullet}$-pyr.

The short C−H bonds are related to the compact nature of the carbon 2s and 2p AOs (Figure 3) which causes optimal bond overlaps and ΔE_{oi} at shorter bond lengths (Table 1). The valence *n*s and *n*p AOs become significantly more extended and diffuse (i.e. the effective size of M increases) and M−H bonds thus elongate, along C, Si, Ge, and Sn (Figure 3: Ge 4s and 4p are not shown; they are only slightly larger than Si 3s and 3p). The origin of this phenomenon is the intraatomic Pauli repulsion[21] of the valence *n*s and *n*p electrons with the increasing number of core shells (Figure 3). The effect is most pronounced for the step from carbon 2p (no p core at all) to silicon 3p (first M with a p core).

The M−H orbital interaction $\Delta E_{oi}(M-H_3)$ is largest for $CH_3^{\bullet}$, but its additional *stabilization upon pyramidalization*, through the $\Delta E_A(M-H_3)$ term, is the *weakest* for this radical. This is again most clearly demonstrated by a comparison of $MH_3^{\bullet}$-plan and $MH_3^{\bullet}$-pyr*: $\Delta E_A(M-H_3)$ is stabilized by −2.9, −4.5, −5.4, and −7.2 kcal/mol along $CH_3^{\bullet}$, $SiH_3^{\bullet}$, $GeH_3^{\bullet}$, and $SnH_3^{\bullet}$, a trend which follows approximately the increasing gain in M−H_3 overlap $\langle np_z|1a_1'\rangle$ (Table 4). The overall $\Delta E_A(M-H_3)$ term is −91.5, −71.5, −79.1, and −65.5 kcal/mol along the $MH_3^{\bullet}$-plan series (Table 4). This trend follows primarily the $ns-1a_1'$ orbital energy gap (5.1, 4.0, 4.9, and 3.4 eV along the $MH_3^{\bullet}$ series) which is controlled by the M-*n*s atomic orbital energies (Figure 2): the smaller the $ns-1a_1'$ energy gap, the smaller the stabilization associated with charge transfer to M-*n*s. The reduction of the M−H_3 overlap $\langle np_z|1a_1'\rangle$ has in addition a weakening effect on $\Delta E_A(M-H_3)$. Together, the interactions in A symmetry lead to a net charge flow from $(H^{\bullet})_3$-$1a_1'$ and M-np_z to M-*n*s (Table 4).

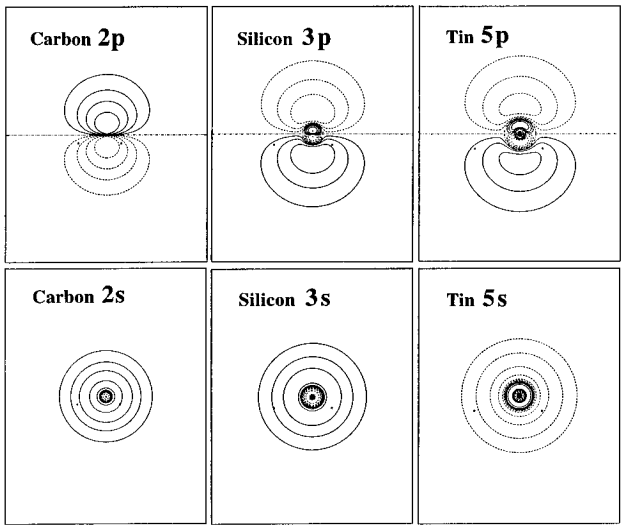

Figure 3. Contour plots of *n*s and *n*p AOs of carbon, silicon, and tin. (Asterisks indicate positions of nuclei in corresponding $MH_3^{\bullet}$. Scan values: 0.0, ±0.02, ±0.05, ±0.10, ±0.2, ±0.5).

The $np_{x,y} \pm 1e_1'$ interaction $\Delta E_E(M-H_3)$ is much stronger than $\Delta E_A(M-H_3)$, but at the same time it *changes much less upon pyramidalization* ($MH_3^{\bullet}$-plan → $MH_3^{\bullet}$-pyr*; eq 8), namely by +1.0, −2.1, −1.1, and −0.7 kcal/mol along $CH_3^{\bullet}$, $SiH_3^{\bullet}$, $GeH_3^{\bullet}$, and $SnH_3^{\bullet}$ (Table 4). Consequently, the change in the overall orbital interaction $\Delta E_{oi}(M-H_3)$ (−1.9, −6.6, −6.5, −7.9 kcal/mol) follows approximately that of the $\Delta E_A(M-H_3)$ term and favors pyramidalization, although only slightly so for $CH_3^{\bullet}$ (Table 4). Note that $\Delta\Delta E_{oi}(M-H_3)$ becomes slightly endothermic (i.e. +0.5 kcal/mol) for $CH_3^{\bullet}$ after M−H elongation ($MH_3^{\bullet}$-pyr* → $MH_3^{\bullet}$-pyr; eq 8). The relative invariance of $\Delta E_E(M-H_3)$ upon pyramidalization is ascribed to a very subtle interplay and mutual cancellation of the trends in overlap $\langle np_x|1e_{1-x}'\rangle$, which is slightly reduced, and the relative orbital energies of M-$np_{x,y}$ and $(H^{\bullet})_3$-$1e_1'$. The fact that $\Delta E_E(M-H_3)$ is significantly larger than $\Delta E_A(M-H_3)$ has its origin in the larger number of valence electrons in E_1 symmetry and in the larger $\langle np_x|1e_{1-x}'\rangle$ overlaps (Table 4, Figure 1). The corresponding electron pair bonds are relatively covalent because of the small $np_{x,y}-1e_1'$ energy gap in combination with the large $np_{x,y} \pm 1e_1'$ splitting. This shows up in orbital populations which are close to one for $np_{x,y}$ and $1e_1'$; only for $SnH_3^{\bullet}$ is there a significant charge transfer of ca. 0.2 e from M to $(H^{\bullet})_3$ (Table 4).

We conclude that the $CH_3^{\bullet}$ radical is planar because of the steric repulsion between the hydrogen ligands whereas electronic effects (i.e. electron pair bonding between central atom and hydrogen ligands) always favor a pyramidal structure.

Table 5. Calculated Homolytic (D_{homo}) and Heterolytic (D_{hetero}) MH_3−Cl Bond Dissociation Energies (in kcal/mol)[a]

	LDA/TZ2P						NL-SCF/TZ2P				literature D_{homo}	
MH_3−Cl	D_{hetero}	ΔZPE	D_{hetero} + ΔZPE	D_{homo}	ΔZPE	D_{homo} + ΔZPE	D_{hetero}	D_{hetero} + ΔZPE[b]	D_{homo}	D_{homo} + ΔZPE[b]	theoretical	exptl
CH_3−Cl	252.2	−4.2	248.0	107.2	−4.8	102.4	236.3	232.1	86.5	81.7	75.8,[c] 78.3,[d] 46.8,[e] 83.0,[f] 83.2[g]	83.4,[h] 82.4[i]
SiH_3−Cl	222.4	−2.4	220.0	124.4	−3.1	121.3	212.3	209.9	108.7	105.6	104.9,[j] 109.7,[g] 109[k]	125.5,[h] 113[l]
GeH_3−Cl	209.9	−1.9	208.0	114.3	−2.8	111.5	199.2	197.3	99.0	96.2		
SnH_3−Cl	196.8	−2.1	194.7	111.4	−4.2	107.2	187.6	185.5	97.8	93.6		

[a] D_{hetero} = energy change for $MH_3Cl \rightarrow MH_3^+ + Cl^-$; D_{homo} = energy change for $MH_3Cl \rightarrow MH_3^\bullet + Cl^\bullet$. [b] ΔZPE from LDA/TZ2P frequencies. [c] MP4/6-311G(d,p)//MP2/6-311G(d,p)+ΔZPE: ref 5a. [d] MP2/6-311G(d,p)+ΔZPE: ref 5a. [e] HF/6-311G(d,p)//MP2/6-311G(d,p)+ΔZPE: ref 5a. [f] G2: ref 6l. [g] CBS-Q: ref 6l. [h] Calculated with ΔH_f^{298} values from ref 3a. [i] Calculated with ΔH_f^{298} values from ref 3b. [j] Obtained from experimental $D(CH_3-Cl)_{298}$ + MP4/6-31G*//HF/3-21G*+ΔZPE value of ΔH_r for $SiH_3Cl + CH_3^\bullet \rightarrow SiH_3^\bullet + CH_3Cl$: ref 6f. [k] G2: ref 6i,m. [l] Reference 4b.

C. MH_3Cl Geometry and M−Cl Bond Dissociation Energy. Now, we come to the MH_3Cl molecules in which the $MH_3^\bullet$ radicals act as building blocks. The M−Cl and M−H bonds *expand* by ca. 0.6 Å, and the MH_3 fragment becomes ca. 2° *less* pyramidal for heavier M: d_{MCl} = 1.779, 2.034, 2.129, and 2.361 Å and H−M−H angle β = 110.52, 110.30, 111.62, and 112.40° along CH_3-Cl, SiH_3Cl, GeH_3Cl, and SnH_3Cl (Table 1, NL-SCF/TZ2P). The homolytic M−Cl bond dissociation energy rises steeply in going from C−Cl to Si−Cl and then decreases more moderately in going from Si−Cl to Sn−Cl: D_{homo} + ΔZPE is 81.7, 105.6, 96.2, and 93.6 kcal/mol for CH_3−Cl, SiH_3−Cl, GeH_3−Cl, and SnH_3−Cl, respectively (Table 5, NL-SCF/TZ2P). The corresponding heterolytic M−Cl bond dissociation energies are significantly higher: D_{hetero} + ΔZPE is 232.1, 209.9, 197.3, and 185.5 kcal/mol along the same series (Table 5, NL-SCF/TZ2P). Thus, isolated MH_3−Cl dissociates in all four cases preferentially in a homolytic fashion.

Our results are in excellent agreement with the available literature data (Tables 2 and 5).[2−6,9b] Both theoretical (HF/ECP1*)[6b] and experimental (MW, IR)[2] studies confirm the ca. 0.6 Å M−Cl and M−H bond elongation and the ca. 2° decrease of the H−M−H angle β (Table 2). The trend of the homolytic bond dissociation energy (D_{homo} + ΔZPE) is also fully corroborated for CH_3Cl and SiH_3Cl (Table 5); to our knowledge no previous data are available for GeH_3Cl and SnH_3Cl. Our NL-SCF CH_3−Cl bond dissociation energy of 81.7 kcal/mol is only ca. 2 kcal/mol lower than experimental (83.4 and 82.4 kcal/mol) or G2 values (83.0 kcal/mol); for comparison, the HF, MP2, and MP4 calculations underestimate the CH_3−Cl bond dissociation energy by 37, 5, and 8 kcal/mol, respectively (Table 5). Our NL-SCF SiH_3−Cl bond dissociation energy of 105.6 kcal/mol is essentially equal to the accurate value of 104.9 kcal/mol obtained by Luke *et al.*[6f] by adding their MP4/6-31G*//HF/3-21G* + ΔZPE energy change for the isogyric reaction $SiH_3Cl + CH_3^\bullet \rightarrow SiH_3^\bullet + CH_3Cl$ to the experimental CH_3−Cl bond dissociation energy. The G2 value of 109 kcal/mol is somewhat higher. Thus, the theoretical studies are in support of an SiH_3−Cl bond dissociation energy (105−109 kcal/mol) which is 4−21 kcal/mol lower than the experimental values (113−126 kcal/mol; Table 5).

D. MH_3Cl Bonding Mechanism. *Why* does the MH_3−Cl bond strength increase at first and then decrease whereas the M−Cl bond length increases continuously along M = C, Si, Ge, and Sn? To answer this, a detailed analysis of the bonding mechanism has been carried out (Table 6). The overall M−Cl bond energy $\Delta E = -D_{homo}$ is divided into two terms (eq 9).

$$MH_3^\bullet + Cl^\bullet \rightarrow MH_3Cl \qquad \Delta E = \Delta E_{prep} + \Delta E_{int} \quad (9)$$

The preparation energy ΔE_{prep} is the energy required to deform $MH_3^\bullet$ to its geometry in MH_3Cl. The actual interaction ΔE_{int} between the prepared $MH_3^\bullet$ and $Cl^\bullet$ is composed of the steric repulsion ΔE^0 and the attractive orbital interaction ΔE_{oi} (section 2B). The orbital interaction ΔE_{oi} is mainly (≳90%) provided by the polar electron pair bond between the SOMOs of $MH_3^\bullet$ and $Cl^\bullet$, $2a_1 \pm 3p_z$ (Figure 4). The steric interaction ΔE^0 is dominated by the Pauli repulsion between closed shells: $1a_1 \pm 3s$ (or $1a_1 \pm 3p_z$) and $1e_1 \pm 3p_{x,y}$ (Figure 4).

The M−Cl bond lengths are determined by the balance between the repulsive ΔE^0 and attractive ΔE_{oi}. Both interaction terms have their onset or optimum (for ΔE_{oi}) at still longer d_{MCl} along M = C, Si, Ge, and Sn, because of a similar behavior of the corresponding MH_3−Cl orbital overlaps. The origin of this phenomenon is again intraatomic Pauli repulsion[21] which causes valence orbitals of M and thus $MH_3^\bullet$ to become more extended and diffuse (Figure 3) when the number of core shells increases (see also section 3B).

Table 6. Analysis of the M−Cl Bonding Mechanism between $MH_3^\bullet$ and $Cl^\bullet$ in MH_3Cl[a]

	CH_3−Cl	SiH_3−Cl	GeH_3−Cl	SnH_3−Cl
Energy (in kcal/mol)[a,b]				
ΔE^0	82.4	82.7	67.8	49.8
ΔE_{oi}	−175.1	−191.4	−166.9	−147.8
ΔE_{int}	−92.7	−108.7	−99.1	−98.0
ΔE_{prep}	6.2	0.0	0.1	0.2
ΔE	−86.5	−108.7	−99.0	−97.8
Orbital Energy Gap (in eV)				
$2a_1-3p_z$	3.8	4.6	4.7	4.9
Fragment Orbital Overlaps $\langle MH_3\|Cl\rangle$[c]				
$\langle 1a_1\|3s\rangle$	0.16	0.15	0.14	0.12
$\langle 1a_1\|3p_z\rangle$	0.28	0.23	0.23	0.19
$\langle 2a_1\|3p_z\rangle$	0.34	0.34	0.33	0.32
$\langle 1e_{1-x}\|3p_x\rangle$	0.15	0.12	0.11	0.09
Fragment Orbital Populations (in e)[d]				
$MH_3^\bullet$ $P(2a_1)$	0.83	0.54	0.56	0.44
$Cl^\bullet$ $P(3p_z)$	1.17	1.44	1.42	1.53

[a] NL-SCF/TZ2P; ΔE_{int} decomposition: NL-P/TZ2P scaled to fit with NL-SCF/TZ2P result. [b] ΔE^0 = steric interaction, ΔE_{oi} = orbital interaction (comes from ≳90% from A_1 symmetry), ΔE_{int} = net interaction between $MH_3^\bullet$ and $Cl^\bullet$, ΔE_{prep} = preparation energy, required to deform $MH_3^\bullet$ to its geometry in the overall molecule, ΔE = overall energy change for $MH_3^\bullet + Cl^\bullet \rightarrow MH_3Cl$ (see eq 9). [c] Overlaps between $MH_3^\bullet$ and $Cl^\bullet$ orbitals. [d] $P(\varphi)$ is the gross Mulliken population which fragment orbital φ acquires in the overall molecule.

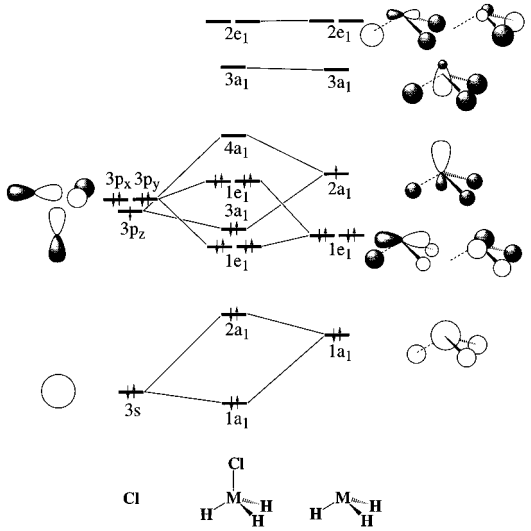

Figure 4. Orbital interaction scheme for MH_3−Cl.

The general trend in the MH_3−Cl bond energy is set by the orbital interaction ΔE_{oi} (=−175.1, −191.4, −166.9, and −147.8 kcal/mol) which gives rise to the order C < Si > Ge > Sn (Table 6). The orbital interaction ΔE_{oi} correlates to a certain degree with the $2a_1-3p_z$ energy gap (=3.8, 4.6, 4.7, 4.9 eV) which reflects the trend in M-np_z AO energies (Figure 2) and increases steeply from M = C to Si (Figure 5 and Table 6).[25] Consequently, the electron originating from the $MH_3^{\bullet}$-$2a_1$ experiences a stronger stabilization when it enters the bonding $2a_1 + 3p_z$ (i.e. MH_3Cl-$3a_1$), in spite of a reduced $2a_1 \pm 3p_z$ interaction (Figure 5). Thus, the M−X bond becomes more polarized, as reflected by the increased charge transfer to Cl-$3p_z$ (Table 6). This confirms the finding by Luke *et al.* that the SiH_3−X bond is stronger than the CH_3−X bond for electronegative X due to the lower ionization energy (IE) of the $SiH_3^{\bullet}$ radical.[6f] The $2a_1-3p_z$ energy gap rises only slightly along Si, Ge, Sn (Figure 5).[25] Now, ΔE_{oi} is more sensitive to other factors, e.g. the decreasing $\langle 2a_1|3p_z\rangle$ overlap which weakens the interaction (Table 4). This trend may be further enhanced as the $1a_1 \pm 3p_z$ two-orbital three-electron interaction pushes the Cl-$3p_z$ effectively up in energy, thus causing a smaller $2a_1-3p_z$ energy gap. Together, these effects lead to a further, slight increase of the M−X bond polarization.

The steric repulsion ΔE^0 (=82.4, 82.7, 67.8, and 49.8 kcal/mol) runs counter to the order given by ΔE_{oi} and has the effect to make the overall ΔE the weakest for CH_3−Cl. It remains essentially unchanged in going from CH_3Cl to SiH_3Cl where the $1a_1 \pm 3s$ repulsion is taken over by $1a_1 \pm 3p_z$, as the $MH_3^{\bullet}$-$1a_1$ orbital energy increases (Figure 5). The decrease of ΔE^0 from SiH_3Cl to SnH_3Cl is related to a similar decrease in the $\langle 1a_1|3p_z\rangle$ and $\langle 1e_{1-x}|3p_x\rangle$ overlaps (Table 6). The preparation energy ΔE_{prep} is small and without significant influence on the overall trend: 6 kcal/mol for the pyramidalization of $CH_3^{\bullet}$ and 0 kcal/mol for the heavier $MH_3^{\bullet}$ radicals which are already pyramidal (Table 6).

Summarizing, the MH_3−Cl bond strength ΔE follows initially the increasing M−Cl electronegativity difference (i.e. from C to Si) and then, among others, the decreasing $\langle 2a_1|3p_z\rangle$ overlap which, in combination with the decreasing steric repulsion, leads to the overall order C ≪ Si > Ge > Sn.

Table 7. Analysis of the C−X Bonding Mechanism between $CH_3^{\bullet}$ and $X^{\bullet}$ in CH_3X[a]

	CH_3−F	CH_3−Cl	CH_3−Br	CH_3−I
Geometry (in Å, deg)				
d_{C-X}	1.400	1.778	1.967	2.156
d_{C-H}	1.099	1.095	1.094	1.093
α_{HCX}	108.7	108.2	107.5	107.3
Energy (in kcal/mol)				
ΔE^0	152.0	85.6	55.8	45.0
ΔE_{oi}	−277.9	−179.0	−137.0	−115.4
ΔE_{int}	−125.9	−93.4	−81.2	−70.4
ΔE_{prep}	6.5	5.9	5.4	5.2
ΔE	−119.4	−87.5	−75.8	−65.2
Orbital Energy Gap (in eV)[b]				
$2a_1-np_z$	7.5	3.8	3.0	2.1
Fragment Orbital Overlaps $\langle CH_3\|X\rangle$				
$\langle 2a_1\|np_z\rangle$[b]	0.26	0.34	0.35	0.36
Fragment Orbital Populations (in e)				
$CH_3^{\bullet}$ $P(3a_1)$	0.77	0.83	0.87	0.90
$X^{\bullet}$ $P(np_z)$[b]	1.23	1.17	1.13	1.10

[a] NL-P/TZ2P//NL-SCF/TZ2P; from ref 5a. [b] $np_z = 2p_z$, $3p_z$, $4p_z$, and $5p_z$ for F, Cl, Br, and I, respectively.

Comparison with CH_3−X. We recall that the CH_3−X bond strength ΔE (determined by the orbital interaction ΔE_{oi}) follows the decreasing C−X electronegativity difference (accompanied by a decreasing charge transfer from $CH_3^{\bullet}$-$2a_1$ to X-np_z) which leads to the overall order F ≫ Cl > Br > I (Table 7).[5a] The bond overlap $\langle 2a_1|3p_z\rangle$ runs counter (i.e. increases), but this effect is strongly overruled by the electronegativity trend (Table 7). Thus, bond polarization rather than orbital overlap governs the CH_3−X bond strength.

The apparent difference between the ΔE trends of MH_3−Cl (Table 6) and CH_3−X (Table 7) is the much higher correlation of the latter with the M−X electronegativity difference and bond polarization.[25] The reason is obvious if one compares the trends in the orbital energy gaps $2a_1-3p_z$ (MH_3−Cl) and $2a_1-np_z$ (CH_3−X). The CH_3−X $2a_1-np_z$ gap (=7.5, 3.8, 3.0, and 2.1 eV) changes considerably along X = F, Cl, Br, and I (Table 7). In contrast, the MH_3−Cl $2a_1-3p_z$ gap (=3.8, 4.6, 4.7, 4.9 eV) changes only very slightly, in particular along M = Si, Ge, and Sn (Table 6); therefore, the effect of the decreasing bond overlap $\langle 2a_1|3p_z\rangle$ dominates along the latter.

E. MH_3X LUMO and Reactivity. Finally, we take a closer look to the electronic structure of MH_3X, in particular the $4a_1$ LUMO which plays the important role of acceptor orbital in S_N2 reactions.[23,26] The orbital energy of the MH_3Cl $4a_1$ LUMO decreases by 1.4 eV in going from M = C to Sn, due to the reduced $2a_1-3p_z$ interaction (*vide supra*). This makes the LUMO a still better partner in a donor−acceptor interaction with the HOMO of a nucleophile B^-. Thus, it is to be expected that the activation energy for the $B^- + MH_3Cl$ S_N2

(25) In our approach, orbital energies occur naturally as a measure of (orbital) electronegativities of atoms or groups. Note that the trend in Pauling electronegativities for M, i.e., 2.55, 1.90, 2.01, and 1.96 for C, Si, Ge, and Sn, respectively, follows that of the AO energies and, in particular, that the irregular variation from Si via Ge to Sn correlates with the M-*ns* orbital energy (Figure 2). (b) Electronegativities were taken from: Boyd, R. J.; Markus, G. E. *J. Chem. Phys.* **1981**, *75*, 5385. (c) See also: Pauling, L. *The Nature of the Chemical Bond*; Cornell University Press: Ithaca, NY, 1960; Chapter 3.

(26) Fleming, I. *Grenzorbitale und-Reaktionen organischer Verbindungen;* VCH Verlagsgesellschaft: Weinheim, Germany, 1990.

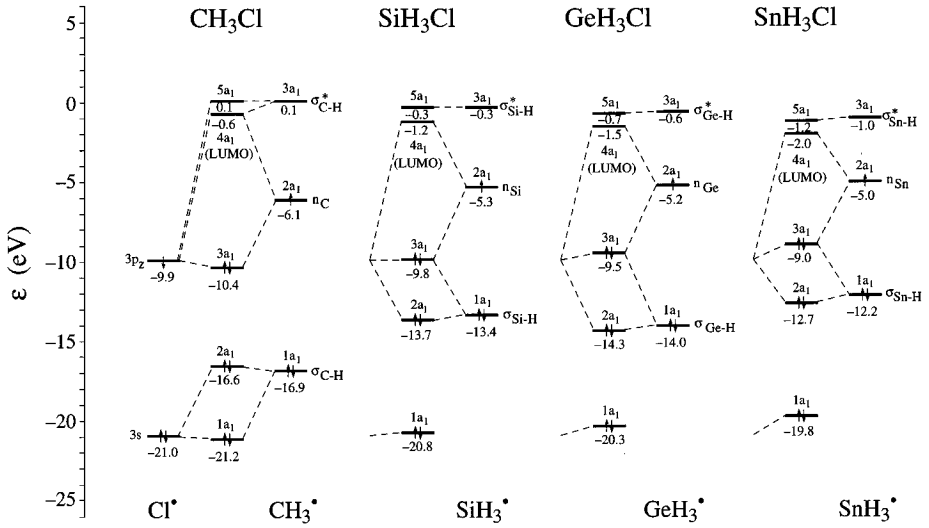

Figure 5. Quantitative A_1 orbital interaction scheme for MH_3-Cl.

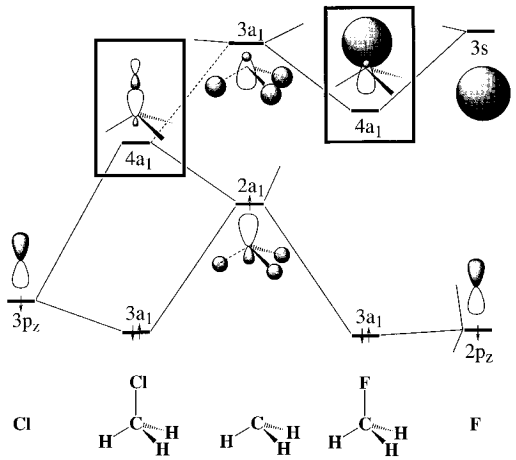

Figure 6. Comparison of the main orbital interactions of CH_3-Cl and CH_3-F.

substitution drops for heavier M and eventually vanishes completely leading to stable pentacoordinate $[B-MH_3-Cl]^-$ intermediates. This is actually confirmed by experimental and theoretical studies (for M = Si).[27] Of course, other factors (e.g. the size of M and orbital overlap) may play an equally important role in determining the course of the $B^- + MH_3Cl$ reactions and more detailed calculations of such reactions are under way to tackle this problem.[28]

Another point concerns the shape of the $4a_1$ LUMO. Recently, we have pointed out that the backside lobe of this LUMO is poorly developed in CH_3Cl, at variance to the "classical" view of a large backside lobe.[22] There are two reasons for this small backside lobe. First, already the $CH_3^{\bullet}$-$2a_1$ has its small lobe at the methyl backside (Figure 6). Nevertheless, the backside lobe of the antibonding $2a_1-3p_z$ combination (i.e. the CH_3Cl $4a_1$ LUMO) could be larger through the renormalization effect. Its amplitude is further diminished by a slight contribution of the $CH_3^{\bullet}$-$3a_1$ which mixes in a bonding fashion with the Cl-$3p_z$ (see Figures 5 and 6).

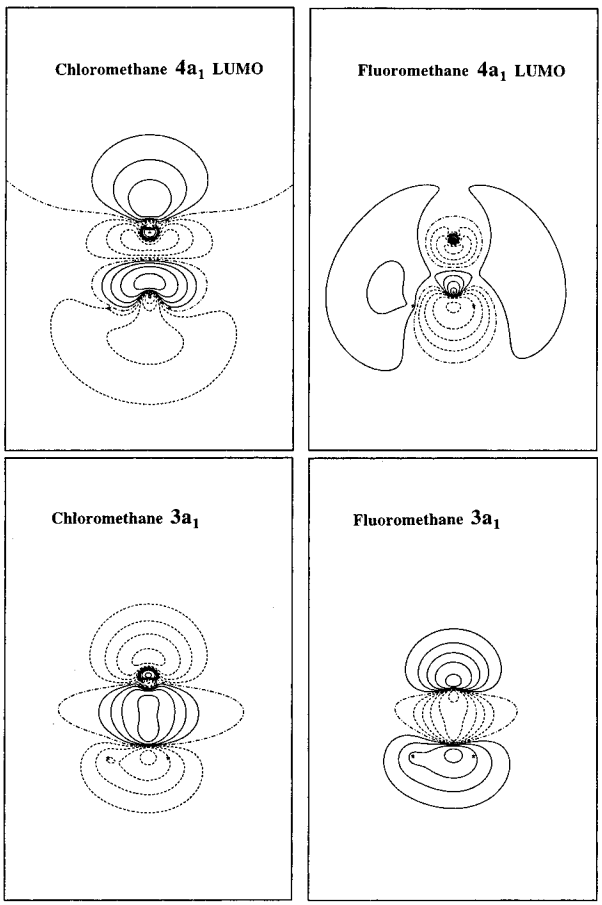

Figure 7. Contour plots of the $4a_1$ LUMOs and $3a_1$ bond orbitals of CH_3Cl and CH_3F. (Asterisks indicate positions of nuclei. Scan values: 0.0, ±0.02, ±0.05, ±0.10, ±0.2, ±0.5.)

The fluoromethane $4a_1$ LUMO has a much higher amplitude backside lobe as shown by the contour plots in Figure 7. Interestingly, the "classical" (i.e. large) backside lobe of the CH_3F $4a_1$ LUMO is *not* the result of a "normal" $2a_1-2p_z$ mixing (i.e. without some admixture of $CH_3^{\bullet}$-$3a_1$). Instead, the CH_3F $4a_1$ LUMO *is* the bonding combination of the empty $CH_3^{\bullet}$-$3a_1$ and the rather diffuse $F^{\bullet}$-3s orbitals (Figure 6)! This unanticipated interaction is due to the very low energy of the fluorine 3s, which is only 0.8 eV above the methyl $3a_1$

(27) See, for example, the following studies and references cited therein: (a) Taketsugu, T.; Gordon, M. S. *J. Phys. Chem.* **1995**, *99*, 8462. (b) Windus, T. L.; Gordon, M. S.; Davis, L. P. Burggraf, L. W. *J. Am. Chem. Soc.* **1994**, *116*, 3568. (c) Ramsden, C. A. *Chem. Soc. Rev.* **1994**, 111. (d) DePuy, C. H.; Damrauer, R.; Bowie, J. H.; Sheldon, J. C. *Acc. Chem. Res.* **1987**, *20*, 127.

(28) Bickelhaupt, F. M.; Ziegler, T.; Schleyer, P. v.R. To be published.

(for comparison, the corresponding chlorine 4s is 5.6 eV above the methyl $3a_1$). Thus, chloromethane and fluoromethane have fundamentally different LUMOs whereas the occupied spectrum is similar (compare the $3a_1$ bond orbitals in Figure 7) in the sense that it arises from corresponding CH_3-X orbital interactions. The CH_3F $4a_1$ LUMO may, however, still transform into the "classical" C−F antibonding $2a_1-2p_z$ when this orbital combination is stabilized by C−F bond elongation (e.g. in an S_N2 transition state), and therefore, the differences between the CH_3F and CH_3Cl LUMOs should not be overrated.

4. Conclusions

The $CH_3^{\bullet}$ radical is planar because of the steric repulsion between the hydrogen ligands. The steric H−H repulsion is much weaker for the heavier central atom homologs in which the ligands are farther removed from each other. Electronic effects (i.e. electron pair bonding between central atom and hydrogen ligands) always favor a pyramidal structure (although only slightly so for the methyl radical) through the additional stabilization of the unpaired electron in M-np_z (Figure 1). This causes an increasing degree of pyramidalization along $SiH_3^{\bullet}$, $GeH_3^{\bullet}$, and $SnH_3^{\bullet}$. Thus, intraatomic Pauli repulsion plays an important role as it is responsible for the occurrence of the increasing number of core shells which cause the central atom M to expand along the $MH_3^{\bullet}$ series.[21]

Our analysis confirms but also adjusts the classical explanation for the trend in $MH_3^{\bullet}$ geometry and inversion barrier as given in Scheme 1. The difference is that the main opposing factor to pyramidalization is the increase in repulsive H−H $\langle 1s|1s\rangle$ overlap and not the loss in $\langle np_{x,y}|1e_1'\rangle$ bonding overlap.

The MH_3-Cl bond strength ΔE increases initially (i.e. from C to Si) with the increasing M−Cl electronegativity difference and then, as the changes in M's electronegativity become small, decreases, following among others the trend of the decreasing SOMO−SOMO bond overlap $\langle 2a_1|3p_z\rangle$; in combination with the decreasing steric repulsion this gives rise to the overall order C ≪ Si > Ge > Sn. The decreasing bond overlap as well as the bond elongation can be ascribed to the expansion and increasing diffuseness of the M-*n*s and *n*p valence orbitals along this series. This is again determined by the intraatomic Pauli repulsion.

The CH_3-X bond strength (X = F, Cl, Br, and I) correlates significantly stronger with the bond polarization. The reason is the larger variation in electronegativity along the halogen atoms if compared to the group 14 atoms.

Acknowledgment. This investigation was supported by the Deutsche Forschungsgemeinschaft (DFG), the Netherlands Organization for Scientific Research (NCF/NWO), and the Natural Sciences and Engineering Research Council of Canada (NSERC). F.M.B. gratefully acknowledges a postdoctoral DFG fellowship.

OM950560K